Real-time Assessment of Human Thermal Comfort Using Image Recognition in Conjunction with a Detailed Numerical Human Model

Abstract

This paper introduces a real-time system for human thermal comfort assessment based on thermal image recognition, sensor fusion and co-simulation. The aim of this work is to provide a framework capable of establishing the best possible representation of a person's thermal state while filling sensor related information gaps by the use of a detailed numerical human model. The latter is used to predict the thermal state for body locations hidden from the IR-camera (e.g. obstacles, clothing) and allows to complete the missing information for local/global thermal comfort predictions. For evaluation purposes, a manikin with flat heated sensors (FHS) simulating human skin is added to an experimental setup. The measured comfort data of all three systems is evaluated to verify the entire system. The paper utilizes a comfort index proposed in DIN EN ISO 14505-2 (2007).

Introduction

Heating and cooling of buildings make up a large proportion of the energy consumption in the world. In the residential and non-residential building sector, HVAC systems account for the largest energy end use comprising heating, ventilation and air conditioning according to Prez-Lombard et al. (2008). Modern air conditioning has also become essential for a higher demand for thermal comfort. In order improve the efficiency of energy use for indoor air conditioning it is important to investigate methods that evaluate people in a building on an individual level in order to establish intelligent control heuristics for HVAC systems. The purpose of these heuristics is on one hand to maintain a maximum level of thermal comfort for everyone present in an indoor environment and on the other hand to minimize energy consumption. Moreover, analyzing an individual's state of thermal comfort on a finer scale and in a real-time fashion promises to yield indications for energy saving potentials.

The use of thermal imaging technology is straightforward. Infrared thermography is a non-invasive, non-destructive tool for measuring surface temperatures that can be adopted for the evaluation of human thermal comfort. Advances in the field of image processing as well as computational image analysis and classification allow for a much more detailed analysis and potential alternative to sensors requiring direct contact with an individual. In order to overcome natural limits of these systems, numerical models can be used to close information gaps caused by missing sensor information. Possible use-cases are intelligent air-conditioning in commercial and residential buildings, vehicle cabins as well as medical applications.

The system presented in this paper relies on multi-modal sensor data and combines multiple hardware-dependent and hardware-independent software components. In order to establish a convenient development and evaluation process, a data server is proposed as a mediator where arbitrary data is exchanged and aggregated. Sensor input data is normalized to a coherent data format which all software components agree upon, thus establishing a robust abstraction layer.

A thermal camera in combination with a motion sensor capable of face and body tracking is used to measure body temperatures. Face and body tracking is based on the work by Smolyanskiy et al. (2014) and Shotton et al. (2013)respectively. In an experimental setup, the thermal camera is mounted above the motion sensor. The desired body regions can be adjusted according to the requirement of the evaluation. Camera calibration is performed so that the positions tracked by the motion sensor can be used for the thermal image. The measured temperatures are converted to an equivalent temperature that combines convection and radiation which can then be correlated with a thermal comfort index called local mean vote (LMV) (DIN EN ISO 14505-2, 2007; Nilsson, 2004). The latter represents a hybrid comfort assessment index that is based on a five-point Bedford scale, which is equivalent to Nilsson's mean thermal vote (MTV) and combines thermal sensation and thermal comfort votes for two different clothing scenarios (1: too cold, 2: comfortably cold, 3: neutral, 4: uncomfortably warm, 5: too warm).

According to Fiala (1998) asymmetrical boundary conditions are much more common in buildings than normally assumed. This requires suitable comfort assessment indices that can evaluate such local phenomena. The equivalent temperature approach (and the related LMV index) contained in DIN EN ISO 14505-2 (2007) in this regard is appropriate for the scenarios described in this work. Furthermore, it contains the description of an objective measurement method that is based on the evaluation of the

dry heat exchange between a human being and its surroundings. A numerical human model (morphable human energy simulator or MORPHEUS) is used to simultaneously predict human skin temperatures. The model combines the mathematical frameworks of Fiala (1998); Fiala et al. (1999, 2001) and Tanabe et al. (2002). The predicted values can be used to fill in regions not seen by the thermal camera. The skin temperatures are also converted to the equivalent temperature and subsequently to the LMV index.

As a third reference system, a manikin with flat heated sensors (FHS) is used. The sensors provide a heat flow in order to maintain a constant surface temperature. This resultant surface temperature can be used to calculate the equivalent temperature and LMV in a similar fashion as done for the thermal camera measurements and the numerical model predictions. An experimental study is conducted based on two example regions of the human body, namely the face and the chest. This is done to demonstrate how the systems perform given a region where the thermal camera can directly see the human skin and a region where it is covered by clothes. The paper draws a comparison between measured equivalent temperatures and comfort evaluations of all three systems.
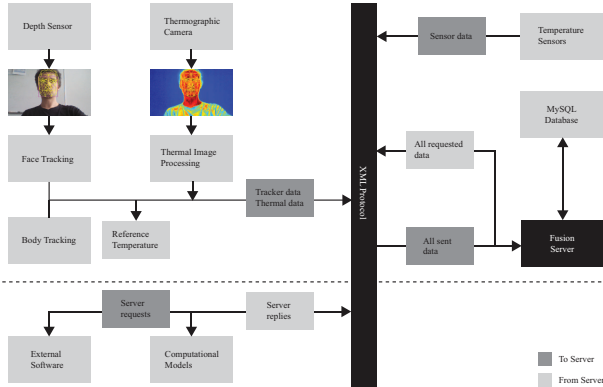
Materials & Methods

System Overview

Figure 1: Schematic of the system architecture

The system presented in this paper is implemented in a highly modular fashion. It is divided into several independent software components responsible for sensor data aggregation, simulation and visualization. Each component communicates over a central data server using common TCP/IP networking. This way it is possible to separate hardware-dependent and hardware-independent software components and greatly simplify the development process. Figure 1 shows a complete system overview and illustrates the data flow between each software component. The following section details each software component.

Data server

The data server functions as a central communication, data aggregation and data visualization platform. It implements a common HTTP interface where data can be exchanged using request-based communication. Moreover, the server maintains an internal hash map with all data being communicated. This hash map implements the described data model. During a measurement, hash maps are added to a measurement stack which can then be stored persistently using ASCII output (e.g. CSV files) or using a database connection. An XML scheme is used for data exchange which utilizes a simple key-value based data model. Each data item is referred to as a *signal*. A *signal* consists of a *name* (which represents the key), a *value* and a *signal group*.

Thermal Image Recognition

In this work, thermal image recognition is used as a mean to evaluate thermal comfort. This requires the detection and tracking of the human body in the thermal image. Two separate camera systems are used. A motion sensor capable of face and body tracking and a thermal camera for surface temperature measurements. Specifically, measurement points in the thermal image are positioned according to the face and skeleton detected using the depth sensor (see Figure 2). The image of the thermal camera needs to be mapped into the coordinate system of the depth sensor in order for the measurement to be accurate. The advantage of two separate camera systems is that the tracking is independent of the thermal camera's resolution or the current temperature.
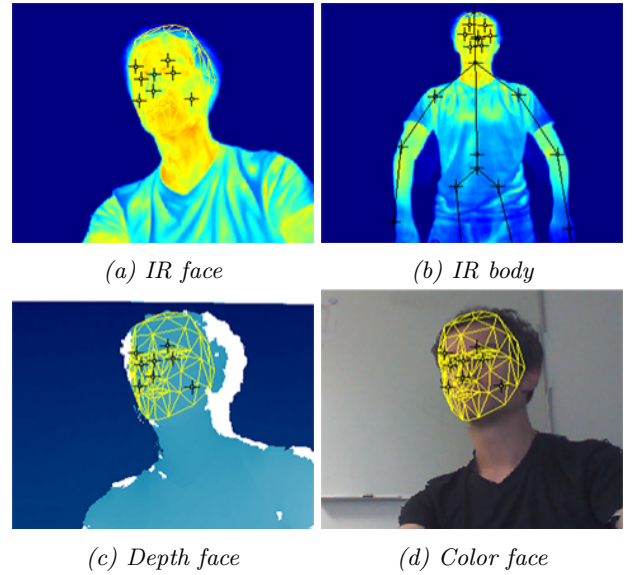

(a) IR face   *(b) IR body*

(c) Depth face   *(d) Color face*

Figure 2: Face tracking and body tracking in the IR, depth and visible domain

Camera System

The thermal camera used for this work is the A35 by FLIR. It is a lower priced thermal camera with an uncooled VOX micro-bolometer and a standalone accuracy of $\pm 5°C$. This accuracy can be greatly improved by using a reference temperature sensor for continuous calibration which will be explained later in this section. The camera has a resolution of 320×256 pixels. The acquisition software uses the Pleora eBUS SDK Technologies (2014) to access the data on the bus.

Reference Temperature Sensor

In order to improve the quality of a low-cost, uncooled thermal camera, a reference temperature sensor is used to improve the temperature measurement accuracy. The reference temperature sensor has a round surface covered in special black varnish that can be seen by the thermal camera. The emissivity of the surface is estimated at $\epsilon = 0.97$. In the thermal imaging software, a reference point can be manually set at the position of the reference temperature sensor. The software then continuously requests the actual measured temperature of the reference sensor from the data server. The thermal camera can then be calibrated so that the measured IR temperature always matches the temperature measured by the sensor. The sensor in the visible and in the experimental setup in the thermal domain can be seen in Figure 3.

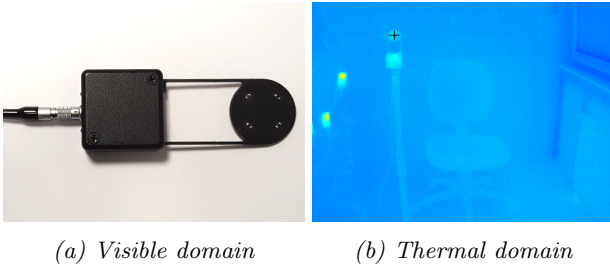(a) Visible domain   (b) Thermal domain

Figure 3: Reference sensor in the visible and in a thermal domain within an experimental setup. The thermal image also shows the reference measurement point set in the thermal image recognition software.

According to Planck's law, the spectral distribution of the radiation from a blackbody can be described using the following formula:

$$W_{\lambda b} = \frac{2\pi hc^2}{\lambda^5(e^{hc/\lambda kT} - 1)} \times 10 - 6[Watt/m^2, \mu m] \quad (1)$$

where $W_{\lambda b}$ is the blackbody spectral radiant emittance at wavelength λ, c is the velocity of light, h is Planck's constant, k is Boltzmann's constant, T is the absolute temperature (K) and λ is the wavelength (μm). This formula can be rearranged in order to determine the temperature T given a radiation value and a electromagnetic frequency (the

spectral range of the FLIR A35 model ranges from 7.5 to 13 μm where atmospheric transmissivity is high). In order to be accurate in real world application, the calculation also needs to include the effects of spectral absorbance (α_λ), spectral reflectance (ρ_λ) and spectral transmittance (τ_λ). The FLIR A35 thermal camera has an internal calibration setting that implements Planck's law resulting in a simplified calculation to convert the thermal pixel values. A value in the pixel matrix can be converted to a temperature value by using a formula combining the internal calibration parameters:

$$T_{[K]} = \frac{B}{ln(\frac{R}{S-O} + F)} \quad (2)$$

where S is the 14-bit digital signal value from the thermal camera, R is the Planck constant, B, F and O are internal camera calibration settings defined in FLIR Systems, Inc. (2014). When given a reference sensor position, this formula is first used to calculate the temperature using the camera factory calibration settings. The temperature is then compared to the actual temperature measured by the reference sensor and an offset value is calculated:

$$t_{offset} = t_{known} - t_{measured} \quad (3)$$

where t_{known} is the value measured by the sensor, $t_{measured}$ is the value seen by the IR camera using factory calibration settings and t_{offset} is the resulting offset. This offset value is then added to all temperatures measured using the camera's factory calibration. The offset value can also be negative in which case it is subtracted from the measured temperatures. This method is valid since offset values are expected to be small and non-linearities are unlikely to significantly influence the result.

Camera calibration

The camera calibration and image registration is performed once using the stereo camera calibration of the OpenCV framework. Since the cameras are mounted statically, calibration is only necessary if physical configurations to the cameras have been changed. The process is initialized by determining the distortion matrix and camera matrix from the circle grid visible in both images. An asymmetrical circle pattern is used to determine the calibration grid. OpenCV uses a blob detector described by Bradski and Kaehler (2008) for detecting the circular shapes on the grid and subsequently establishing the geometric properties of the grid. Multiple image frames with the circle grid appearing in different positions are used in order to establish a sufficient image database for running the calibration. After the calibration procedure the camera matrix along with the respective distortion coefficients can be used to undistort the thermal image and map it into the motion sensor coordinate system.

Once the calibration is finished, points detected using the motion sensor can be directly mapped into the thermal image using the same exact pixel positions. It is convenient to ensure that both image matrices have the same resolution after the camera calibration process so that no additional scaling or coordinate remapping is required.

Pose and Face Detection and Tracking

After the calibration, both the thermal camera and the motion sensor have the same coordinate system, hence coordinates detected using the motion sensor can be used in the thermal image. Figure 2b shows the detected skeleton over the infrared signature of the body. Figure 2d shows the detected 3D face mask mapped onto the infrared signature of the face. Pose tracking is done using a decision forest trained with a database of pre-labeled depth image poses Shotton et al. (2013). The face tracking is based on an active appearance model (AAM) algorithm proposed by Smolyanskiy et al. (2014). Pre-defined measurement points can be attached to detected joints or segments in order to extract temperatures from desired body regions.

Numerical Human Model

A numerical human model is used in connection with a real-time monitor system (Wölki and van Treeck, 2016) to assess the local thermal comfort of body segments hidden from the IR-camera (e.g. clothing, obstacles like desks, etc.). The morphable human energy simulator (MORPHEUS) is implemented in the acausal modeling language Modelica and used in combination with the simulation environment Dymola (see Figure 4). In order to use MORPHEUS in conjunction with the introduced IR-imaging system for the real-time assessment of human thermal comfort, the entire humanoid was exported as a functional mock-up unit (FMU) for co-simulation (Andersson et al., 2016). To benefit from Modelicas acausality and code reusabilty, the entire mathematical model structure was split into independent components. In this regard, the Passive System (PS) component of MORPHEUS approximates the human anatomy via 18 cylindrical elements (arms, hands, legs, etc.) and a single half-sphere for the head. In addition, the cylindrical elements are subdivided into multiple sectors to be able to consider asymmetrical ambient conditions. Depending on the body segment, each sector consists of a combination of seven different tissue materials (bone, muscle, fat, skin, lung, brain, viscera) and is linked to a central blood compartment that handles the heat exchange between the different sectors. The corresponding blood flow model considers the counter-current heat exchange (CCX) between arterial and venous blood streams (extremities and shoulders) that causes a realistic cooling of arterial blood before it enters the tissues

of the different sectors. Furthermore, it rewarms the venous blood streams that return to the central blood compartment, where they form the time-dependent central blood pool temperature. The heat exchange between MORPHEUS and its surroundings is based on convection, radiation, evaporation and respiration. It considers dry and wet heat loss insulation of clothing materials for each body sector (Ambient). In this regard, the original evaporation model of Fiala et al. (1999) was replaced by the corresponding model of Tanabe et al. (2002), which provides a much more Modelica-compliant mathematical structure.

The active thermoregulatory mechanisms that simulate the reactions of the human central nervous system (CNS) towards variations in the human bodys thermal state are contained within the depicted Active System (AS) component. The latter provides the four mechanisms sweating, shivering, vasodilatation and vasoconstriction that prevent the human body from hyper-/hypothermia. The communication between AS and PS is based on afferent/efferent temperature error signals from the skin and hypothalamus, respectively.
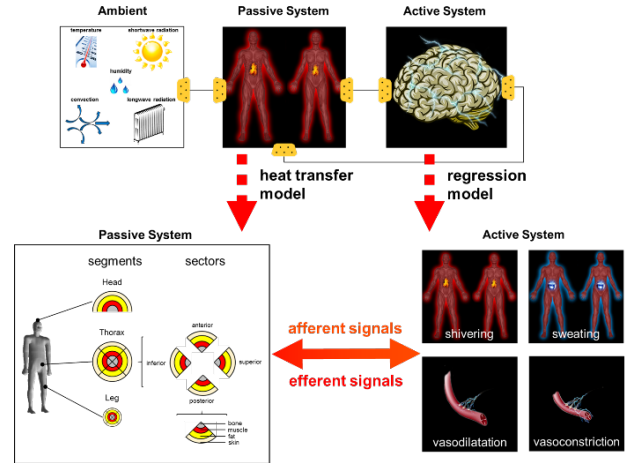

Figure 4: Schematic of MORPHEUS

The humanoid represents an average human being with a body fat percentage of 14.44 %, a body weight of 73.50 kg, a heat exchanging surface of 1.86 m^2, a basal metabolic rate of 87.13 W, a cardiac output of 4.89 l/min, an overall clothing insulation of 1.33 clo and an activity level of 1.2 met.

Thermal Comfort Assessment

Body segment specific thermal comfort is calculated as local mean vote (LMV) according to DIN EN ISO 14505-2 (2007). In this regard, an LMV is rated with discrete values between +1 (too cold and uncomfortable) and +5 (too warm and uncomfortable) with 3 as the neutral point. It is based on the subjective interpretation of the so-called equivalent temperature T_{eq} [$°C$], which represents the temperature of a homogeneous room

in which a local body segment would experience the same dry heat exchange (convection and radiation) with its surrounding micro-climate as in the actual inhomogeneous scenario. The mathematical description of T_{eq} is shown in Equation 4:

$$T_{eq} = T_{sf} - \frac{q_c + q_r}{h_{c,mix} + h_r} \qquad (4)$$

Here, T_{sf} represent the surface temperature of a local body segment [°C], q_c its convective heat loss [W/m^2], q_r its radiative heat loss [W/m^2] and $h_{c,mix}$ and h_r the corresponding mixed convective and radiative heat transfer coefficients [$W/m^2 \ °C$], respectively. The latter were calculated according Fiala et al. (1999). Furthermore, the original T_{eq} equation was expanded by the local evaporative heat loss q_e [W/m^2] calculated with the numerical human model MORPHEUS (see Figure 4).

$$T_{eq} = T_{sf} - \frac{q_c + q_r + q_e}{h_{c,mix} + h_r} \qquad (5)$$

For the calculations with MORPHEUS, the local T_{sf} values of a single body segment were constantly set equal to the local skin temperatures T_{sk} [°C] of the investigated body segments. This was done, because it is assumed that skin temperatures better represent the actual influence of the environment on a persons current thermal state than temperatures measured at the surface of a clothed body sector. Furthermore, to calculate local LMVs via the temperature information from the IR-camera system T_{sf} was replaced by T_{IR} [°C]. Here, the local heat fluxes of the diverse body segments as well as the resulting heat transfer coefficients calculated with MORPHEUS are used as the base for the T_{eq}-calculations.

Measurement of Ambient Conditions
Ambient conditions were recorded inside an office room with north-west orientation, situated on the first floor of a big office building with a comfort measurement device according to DIN EN ISO 7730 (2006) or ASHRAE Standard 55 (2013). The corresponding sensor hardware was manufactured by the German company AHLBORN (AHLBORN, Holzkirchen, Germany). Its single components are listed in Table 1. All physical measurements were recorded at a height of 1.2 m above the floor, which correlates well with the distance between the head and the floor of a sitting person.

Experimental Setup
The office room was conditioned with two chilled beam air conditioning systems manufactured by Airwell Residential, France that were mounted at the ceiling of the office room and an additional mobile air conditioner from Midea Europe GmbH, Germany. The schematic of the entire experimental setup is shown in Figure 5. It can be seen that the camera system is positioned in front of the subject at a

Table 1: Measurement equipment for ambient conditions

Device	Type
data logger	2690 8A
globe thermometer	ZA 9030-FS2
humidity-/temperature sensor	FH A646-E1
thermo-anemometer	FVA605-TA1O

distance of 1.5 m between the person and the camera itself. The depicted reference temperature sensors are positioned beneath the subject at a height of 1.2 m above the floor in order to real-time calibrate the corresponding internal reference temperature of the IR-camera system, thus improving the accuracy of the measured surface temperature information of the subject. In addition, the comfort measurement device (AHLBORN) was positioned directly beneath the subject, below the chilled beam system and outside the detection area of the camera system.
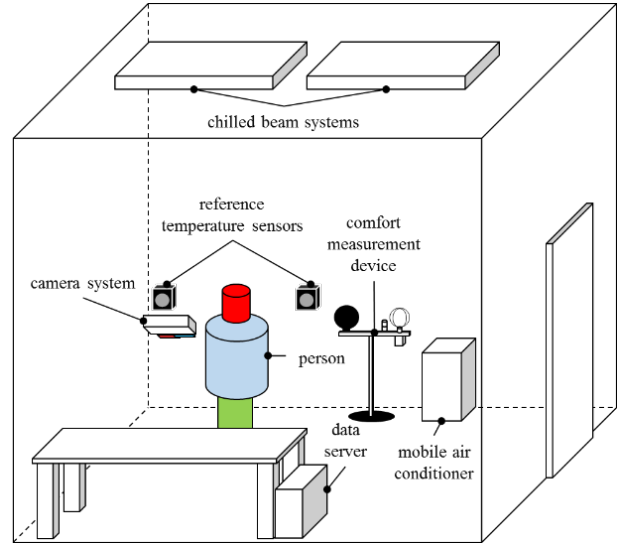

Figure 5: Schematic of the experimental setup

Experiment
For the evaluation of human thermal comfort a preliminary study was carried out. In this regard, the highly dynamic human thermoregulatory responses of a single subject were investigated via a 10 min cool-down cycle that reached 19 °C at its lowest point. The experiment itself started with a 20 min preconditioning phase at an operative temperature (T_{op}) of approximately 22 °C. In order to get an idea on the recovery potential of the subject's energetic state, the cool-down phase was followed by a 15 min rewarming phase in which all air conditioning systems were switched off. No additional heat sources except of the measurement equipment and the subject itself were present in the office room during that phase. Figure 6 shows the corresponding T_{op} signal as well

as the average air velocity (v_a) [m/s] recorded during the experiment at height of 1.2 m above the floor.
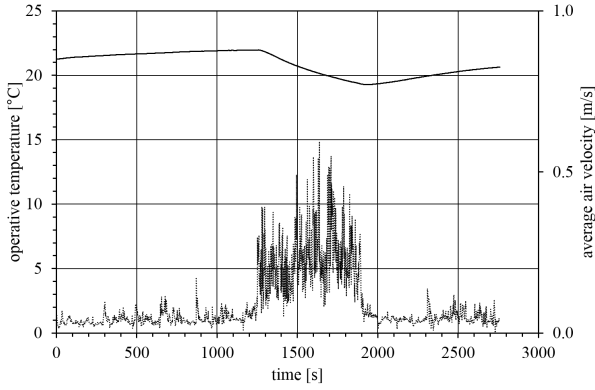

Figure 6: Operative temperature (T_{op}) and average air velocity (v_a) of the office room, measured at a height of 1.2 m above the floor during the 45 min of the experiment

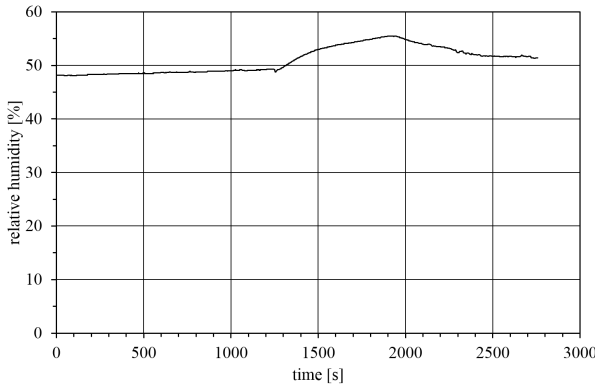The corresponding relative humidity (rh) [%] is depicted in Figure 7.

Figure 7: Relative humidity (rh), measured at a height of 1.2 m above the floor during the 45 min of the experiment

The above mentioned ambient conditions were simultaneously applied to the numerical human model MORPHEUS which simulated the thermo-regulatory reactions of an average human being in real-time. In addition, the humanoid was used to calculate unknown information such as the body segment specific heat transfer coefficients h_c, h_r and their corresponding heat losses Q_c, Q_r and Q_e, required for the calculation of T_{eq} and LMV. During the entire experiment the subject was dressed with a pullover, a t-shirt, a jeans, briefs, socks and shoes which correlates well with the overall clothing insulation value of MORPHEUS according to DIN EN ISO 9920 (2007). The following section gives an example of the results for a clothed (chest) and a naked body sector (face).

Results

Figure 8 shows the T_{eq} results for the naked face. In this regard, the signals $T_{EQ,IR,FACE,0}$ (without Q_e) and $T_{EQ,IR,FACE}$ (including Q_e) represent the T_{eq} signals calculated according to (1) and (2), respectively. In connection with the IR-camera system, T_{sf} was always set equal to T_{IR}. In addition $T_{EQ,MORPHEUS,FACE}$ and $T_{EQ,MORPHEUS,FACE,0}$ are the T_{eq} signals of MORPHEUS calculated with T_{sf} equal to T_{sk}. Finally, $T_{EQ,FHS,FACE}$ represents the measured T_{eq} values of the corresponding flat heated sensor element (FHS).
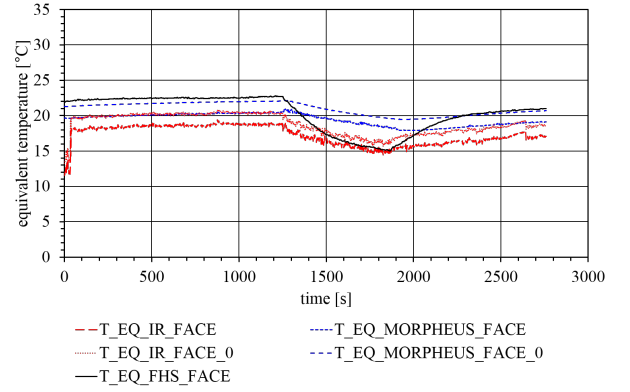

Figure 8: Comparison of the equivalent temperatures (T_{eq}) for the naked face

During the first 20 min of the experiment, a temperature range between 19.5 °C-22.6 °C for the different T_{eq} signals can be obtained. In this connection, the unstable T_{eq} results related to the IR-camera system during the first 33 seconds of the experiment can be neglected. They are the result of the initialization phase of the temperature tracking algorithm. Nevertheless, a constant offset between the T_{eq} signals of the same category (e.g. $T_{EQ,IR,FACE,0}$ vs. $T_{EQ,IR,FACE}$) is present. In addition, $T_{EQ,IR,FACE,0}$ and $T_{EQ,MORPHEUS,FACE}$ are nearly identical during the first 20 min of the experiment. Furthermore, $T_{EQ,MORPHEUS,FACE,0}$ and $T_{EQ,FHM,FACE}$ show good agreement within the first 20 min and the last 10 min of the experiment. During the 10 min cool-down cycle all T_{eq} signals show decreasing amplitudes. In this regard, the steepest T_{eq} decline can be obtained for $T_{EQ,FHS,FACE}$. However, its minimum is in good agreement with $T_{EQ,IR,FACE}$. Furthermore, during the final 25 min of the experiment $T_{EQ,MORPHEUS,FACE}$ and $T_{EQ,MORPHEUS,FACE,0}$ are constantly above $T_{EQ,IR,FACE}$ and $T_{EQ,IR,FACE,0}$. Finally, it can be seen that $T_{EQ,FHM,FACE}$ covers the entire bandwidth of the remaining T_{eq} signals. The comparison between the T_{eq} signals of the clothed chest is shown in Figure 9.
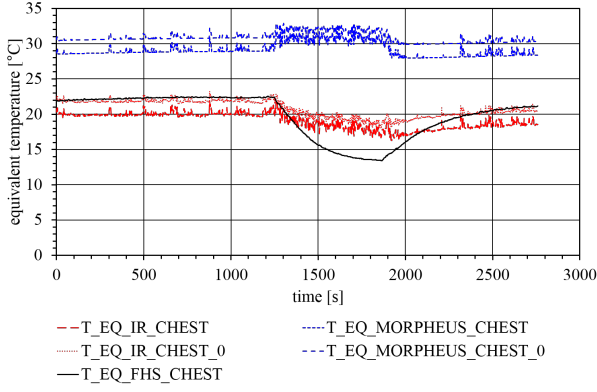
Figure 9: Comparison of the equivalent temperatures (T_{eq}) for the clothed chest

A clear difference between the T_{eq} results calculated with MORPHEUS and the remaining T_{eq} signals can be obtained for the entire experimental phase. The offset between $T_{EQ,MORPHEUS,CHEST}$ and $T_{EQ,IR,CHEST}$ as well as $T_{EQ,MORPHEUS,CHEST,0}$ and $T_{EQ,IR,CHEST,0}$ is approximately 9 K during the 20 min preconditioning phase. It increases during the 10 min cool-down cycle to a maximum of about 14 K. In addition, the T_{eq} signals of MORPHEUS show an inverse behavior during the cool-down and the rewarming phase when compared to the T_{eq} signals of the IR-camera system and the FHS. The latter, however, shows the lowest amplitude of all the signals during the cool-down cycle, but correlates well with $T_{EQ,IR,CHEST}$ during the first 20 min preconditioning and the final 7 min of the experiment. The corresponding LMVs for both body segments are illustrated in Figures 10-11.
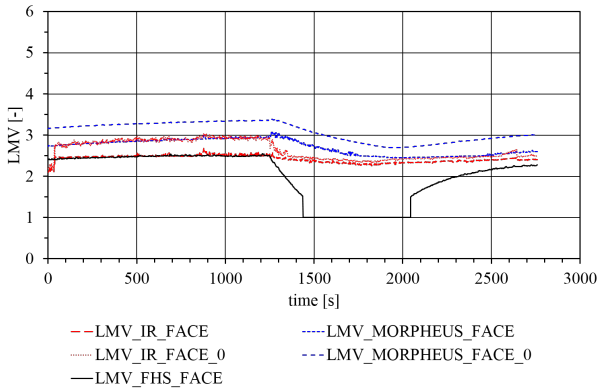

Figure 10: Comparison of the local mean votes (LMV) for the face segment

Except for the FHS, the resulting LMVs are concentrated around the neutral value of +3 (+2.5 to +3.5). However, the FHS shows a decreasing amplitude during the cool-down cycle which immediately drops down to a value of +1 after 23 min. During the subsequent 10 min it constantly

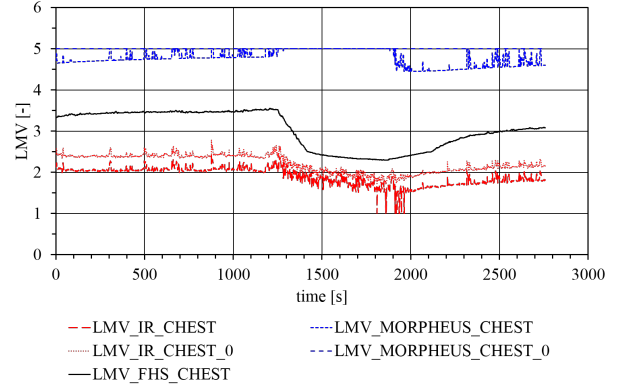remains on this level and nearly approaches the value of $LMV_{IR,face}$ at the end of the experiment.

Figure 11: Comparison of the local mean votes (LMV) for the chest segment

The comparison of the predicted LMVs for the chest segment, significantly differ from each other. Here, the predicted LMVs range from +2 ($LMV_{IR,chest}$) to +5 ($LMV_{MORPHEUS,chest,0}$), whereas the $LMV_{FHS,chest}$ values are mainly fluctuating around +3. Furthermore, the $LMV_{MORPHEUS,chest}$ signal once more shows an inverse behavior when compared to the remaining LMVs during the cool-down and rewarming phase. The local skin (T_{sk}) and surface temperatures (T_{sf}) of the face simulated with MORPHEUS or measured with the IR-camera system/FHS are depicted in Figure 12.
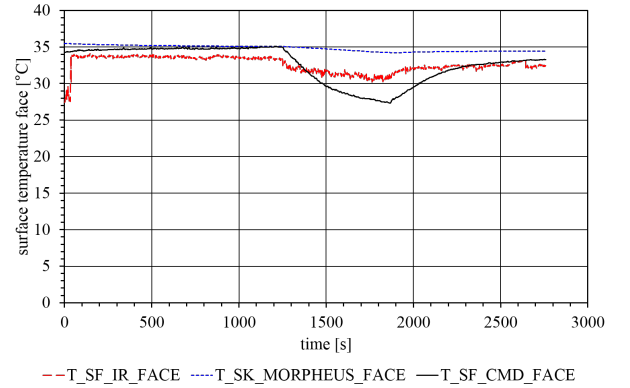

Figure 12: Comparison between the local skin and surface temperatures for the face segment

A good match between $T_{sk,MORPHEUS,face}$ (35 °C to 36 °C) and $T_{sk,FHS,face}$ (34.5 °C to 35 °C) is present during the entire preconditioning phase. During that time, the measured $T_{sf,IR,face}$ of the IR-camera system, however, is constantly below the remaining values (33.6 °C to 34 °C). The corresponding difference between $T_{sk,MORPHEUS,face}$ and $T_{sf,IR,face}$ is approximately 2 K and increases to a maximum difference of 4.15

K after 30 min of the experiment. Nevertheless, the same dynamic behavior can be observed for all the different temperature signal. As could be demonstrated for the T_{eq} signal, $T_{sf,FHS,face}$ shows the highest dynamics and the steepest temperature gradients. The corresponding results of the chest segment are depicted in Figure 13.
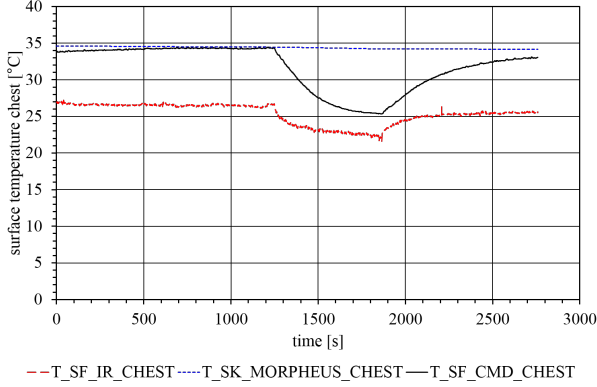

Figure 13: Comparison bewteen the local skin and surface temperatures for the chest segment

The figure above once more shows a high correlation between $T_{sk,MORPHEUS,chest}$ (35 °C) and $T_{sk,FHS,chest}$ (34 °C to 35 °C) during the initial 20 min. However, a big difference between both signals occurs during the cool-down phase. Here, $T_{sk,FHS,chest}$ significantly decreases down to a value of approximately 25.47 °C, which leads to a difference between $T_{sk,MORPHEUS,chest}$ and $T_{sk,FHS,chest}$ of 8.74 K. During the rewarming phase, however, $T_{sk,FHS,chest}$ increases and nearly converges to $T_{sk,MORPHEUS,chest}$. The difference between $T_{sk,IR,chest}$ and $T_{sk,MORPHEUS,chest}$ during the preconditioning phase is approximately 7.6 K and increases during the cool-down cycle up to a maximum of 12.6 K. Results of the radiative heat transfer coefficients (h_r) calculated with MORPHEUS for both, face and chest, are depicted in Figure 14.
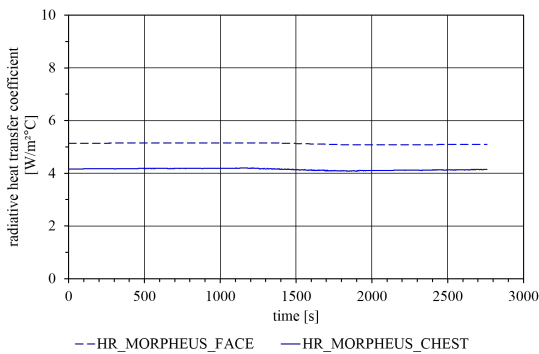

Figure 14: Radiative heat transfer coefficients (h_r), calculated with MORPHEUS for the face and chest

In this connection, $h_{r,MORPHEUS,face}$ (5.10 W/m^2 °C - 5.14 W/m^2 °C) is constantly above the values of the chest (4.09 W/m^2 °C - 4.18 W/m^2 °C), indicating nearly constant surface temperatures of the surrounding walls.

The corresponding mixed convective heat transfer coefficients (h_{cmix}) calculated with MORPHEUS for the face and chest segment are illustrated in Figure 15.
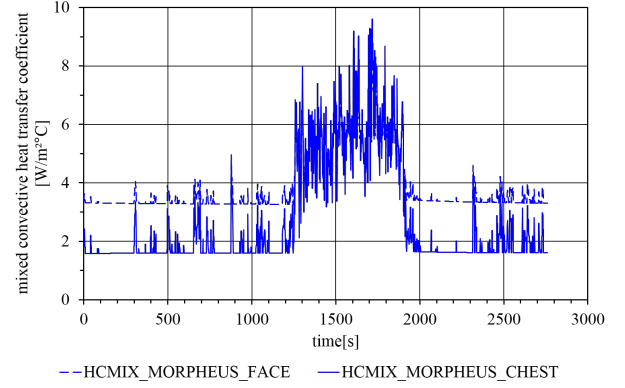

Figure 15: Convective heat transfer coefficients (h_{cmix}), calculated with MORPHEUS for the face and chest

As for the radiative heat transfer coefficient, $h_{cmix,MORPHEUS,face}$ (3.27 W/m^2 °C - 8.24 W/m^2 °C) is mainly higher than $h_{cmix,MORPHEUS,chest}$ (1.59 W/m^2 °C - 9.60 W/m^2 °C). However, during the cool-down phase the maximum $h_{cmix,MORPHEUS,chest}$ is slightly higher than the corresponding $h_{cmix,MORPHEUS,face}$. In addition both signals show highly fluctuating amplitudes, which tremendously increase during the cool-down phase.

Figures 16-17 depict the local heat losses (Q_{loc}) of the face and chest, calculated with MORPHEUS.
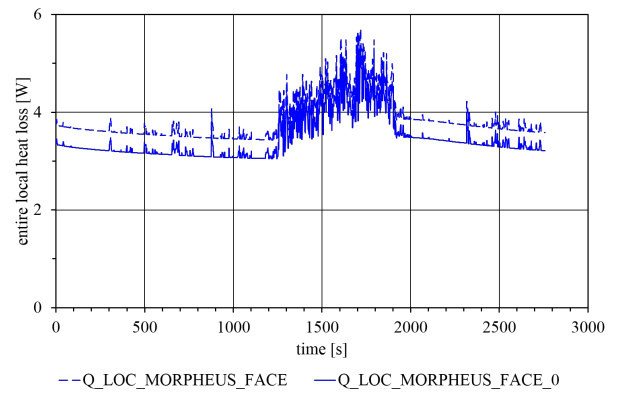

Figure 16: Local heat losses of the face, calculated with MORPHEUS with and without evaporation (Q_e)

In this regard, a constant offset between $Q_{loc,MORPHEUS,face,0}$ and $Q_{loc,MORPHEUS,face}$ is present (1 W). In addition, a highly dynamic behavior for both signals is present, especially during the cool-down phase, during which the heat losses are the highest (5.32 W - 5.7 W). The corresponding local heat losses of the chest, calculated with MORPHEUS are shown below. As for the face segment, $Q_{loc,MORPHEUS,chest,0}$ is once more lower than $Q_{loc,MORPHEUS,chest}$. Furthermore, both signals are much more stable and show less sensitivity towards fluctuating ambient conditions which is reflected in the much lower dynamics of the signal amplitudes, when compared to the face signals.
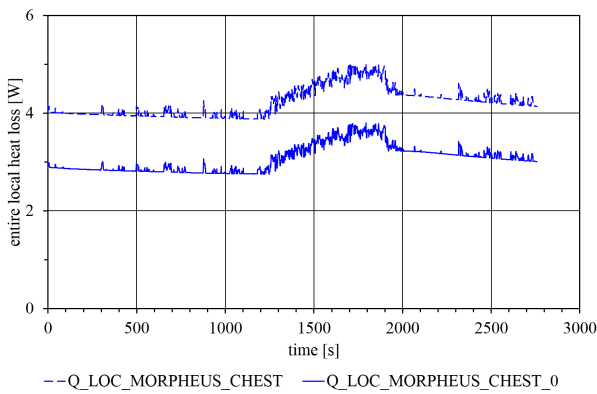

Figure 17: Local heat losses of the chest, calculated with MORPHEUS with and without evaporation (Q_e)

Discussion

Figure 8 generally showed a good correlation between the T_{eq} values calculated with the numerical human model MORPHEUS and equivalent temperatures that are based on measurements with the introduced IR-camera system. However, this is not surprising, because both of them are based on the local heat transfer coefficients h_r and h_{cmix} as well as on the local heat losses Q_{loc} calculated by MORPHEUS. Nevertheless, the independent FHS-signal covers nearly the same T_{eq} range, thus indicating the general correctness of this approach. Furthermore, the FHS shows slightly higher dynamics during the cool-down and rewarming phase than the IR-camera system and MORPHEUS. This is reflected in the steeper T_{eq} gradients during that intervals. The equivalent temperatures of the chest, however, are completely different between the measurement systems and the numerical model MORPHEUS (Figure 9). In this regard, T_{eq} calculated on the base of the IR-temperature signal T_{IR} measured at the clothing surface of the subject is much lower than the skin temperature T_{sk} of the chest simulated by MORPHEUS (Figure 13). Consequently, the corresponding T_{eq} values of that region are lower,

too. The much higher and much more stable T_{eq} values predicted by MORPHEUS for the chest region are the consequence of using T_{sk} values instead of clothing surface temperatures T_{sf}. The latter are much more sensitive towards fluctuations in operative temperature T_{op} and air velocity v_{air} (Figure 6), leading to a nearly identical signal behavior. The insulating effect of clothing is clearly demonstrated in Figure 17 in which the local heat losses of the chest $Q_{loc,MORPHEUS,chest}$ and $Q_{loc,MORPHEUS,chest,0}$ are shown. In this regard, the additional cooling effect of evaporation becomes apparent. The latter is reflected in the lower signal amplitude of $Q_{loc,MORPHEUS,chest}$ when compared to $Q_{loc,MORPHEUS,chest,0}$.

The maximum difference of approximately 4.15 K between the face temperature predicted with MORPHEUS and the measured skin temperature of the IR-camera system during the cool-down phase can be partly addressed to the differences in the initial face temperatures. In this connection the measured T_{IR} signal of the face is approximately 2 K below the calculated face temperature of MORPHEUS. This, however, can be related to individual specific differences in skin blood flow. The latter is closely linked to the vasomotive reactions of the subject and might be different from the MORPHEUS model configured with the anatomical information of an average human being. In this regard, a possible improvement of MORPHEUS' temperature predictions might be achieved by adapting the anatomical part of the humanoid to the body constitution of the investigated subject. This, however, would influence the energy exchange between the humanoid and its surrounding, thus leading to an increased accuracy of local skin temperature predictions. Nevertheless, it is interesting to see that the simulated and the measured skin temperatures for the face are generally in good agreement. Furthermore, it might be beneficial to investigate the heat transfer coefficient h_r and h_{cmix} which might represent an additional source of error in connection with the prediction of local skin temperatures for uncovered body segments. Finally, the big differences in the predicted local mean votes (LMV) for the chest region, can be related to the different surface temperatures used to calculate the corresponding LMVs. Again, the difference between the measured chest temperature of the subject (clothing surface) and the skin temperature of the chest calculated with MORPHEUS cause a deviation in local thermal comfort prediction of about 4 units (Figure 11). In this regard, the LMV calculated on the base of T_{IR} predicts a minimum comfort of +1 (too cold and uncomfortable) during the cool-down phase whereas MORPHEUS predicts a value of +5 (too warm and uncomfortable). In this experiment, however, an immediate cooling of the chest covered with a pullover might probably be

unrealistic. Consequently the LMV predicted with MORPHEUS seems to be more realistic than the LMV predicted on the base of T_{IR}.

Conclusion

This paper introduced a system for the real-time assessment of human thermal comfort. An extensible approach for multi-modal sensor fusion was proposed and evaluated on an experimental basis. It was shown that using numerical human models in combination with contact-less thermal imaging might be beneficial for the assessment of human thermal comfort on a local level in cases where sensor coverage is incomplete or undesirable. Additionally, the paper showed the real-time interaction between the numerical model MORPHEUS and the real measured ambient conditions. Further studies are necessary to improve the prediction quality of the humanoid in terms of temperature information of individual persons.

Acknowledgement

References

Andersson, C., J. Åkesson, and C. Führer (2016). PyFMI: A Python package for simulation of coupled dynamic models with the functional mock-up interface. Technical report, Centre for Mathematical Sciences, Lund University.

ASHRAE Standard 55 (2013). *Thermal environmental conditions for human occupancy.*

Bradski, G. and A. Kaehler (2008). *Learning OpenCV: Computer vision with the OpenCV library.* " O'Reilly Media, Inc.".

DIN EN ISO 14505-2 (2007). *Ergonomics of the thermal environment-Evaluation of thermal environments in vehicles-Part 2: Determination of the equivalent temperature (ISO 14505-2:2005).*

DIN EN ISO 7730 (2006). *Ergonomics of the thermal environment: Analytical determination and interpretation of thermal comfort using calculation of the PMV and PPD indices and local thermal comfort criteria (ISO 7730:2005).*

DIN EN ISO 9920 (2007). *Ergonomics of the thermal environment: Estimation of thermal insulation and water vapour resistance of a clothing ensemble (ISO 9920:2007).*

Fiala, D. (1998). *Dynamic simulation of human heat transfer and thermal comfort.* Ph. D. thesis, HOCHSCHULE FÜR TECHNIK.

Fiala, D., K. Lomas, and M. Stohrer (1999). A computer model of human thermoregulation for a wide range of environmental conditions: the passive system. *J Appl Physiol 87*, 1957–1972.

Fiala, D., K. J. Lomas, and M. Stohrer (2001). Computer prediction of human thermoregulatory and temperature responses to a wide range of environmental conditions. *Int J Biometeorol 45*, 143–159.

FLIR Systems, Inc. (2014). Users manual FLIR Ax5 series.

Nilsson, H. (2004). Comfort climate evaluation with thermal manikin methods and computer simulation models (phd thesis). *Royal Institute of Technology, Sweden. University of Gävle, Sweden.*

Prez-Lombard, L., J. Ortiz, and C. Pout (2008). A review on buildings energy consumption information. *Energy and Buildings 40*(3), 394 – 398.

Shotton, J., T. Sharp, A. Kipman, A. Fitzgibbon, M. Finocchio, A. Blake, M. Cook, and R. Moore (2013). Real-time human pose recognition in parts from single depth images. *Communications of the ACM 56*(1), 116–124.

Smolyanskiy, N., C. Huitema, L. Liang, and S. E. Anderson (2014). Real-time 3d face tracking based on active appearance model constrained by depth data. *Image and Vision Computing 32*(11), 860–869.

Tanabe, S., K. Kobayashi, J. Nakano, Y. Ozeki, and M. Konishi (2002). Evaluation of thermal comfort using combined multi-node thermoregulation (65MN) and radiation models and computational fluid dynamics (CFD). *Energy and Buildings 34*, 637–646.

Technologies, P. (2014). Data sheet ebus sdk. Technical report.

Wölki, D. and C. van Treeck (2016). Real-time monitor for the assessment of human thermal comfort based on PyFMI, Modelica and OpenGL. In *IAQVEC, 9th International Conference on Indoor Air Quality and Energy Conservation in Buildings*, Incheon Songdo, Korea.